

Diffuse gas properties and stellar metallicities in cosmological simulations of disc galaxy formation

Federico Marinacci^{1,2*}, Rüdiger Pakmor¹, Volker Springel^{1,2}
and Christine M. Simpson¹

¹Heidelberger Institut für Theoretische Studien, Schloss-Wolfsbrunnengasse 35, 69118 Heidelberg, Germany

²Zentrum für Astronomie der Universität Heidelberg, Astronomisches Recheninstitut, Mönchhofstr. 12-14, 69120 Heidelberg, Germany

Accepted 2014 June 6. Received 2014 June 5; in original form 2014 March 19

ABSTRACT

We analyse the properties of the circum-galactic medium and the metal content of the stars comprising the central galaxy in eight hydrodynamical ‘zoom-in’ simulations of disc galaxy formation. We use these properties as a benchmark for our model of galaxy formation physics implemented in the moving-mesh code AREPO, which succeeds in forming quite realistic late-type spirals in the set of ‘Aquarius’ initial conditions of Milky Way-sized haloes. Galactic winds significantly influence the morphology of the circum-galactic medium and induce bipolar features in the distribution of heavy elements. They also affect the thermodynamic properties of the circum-galactic gas by supplying an energy input that sustains its radiative losses. Although a significant fraction of the heavy elements are transferred from the central galaxy to the halo, and even beyond the virial radius, enough metals are retained by stars to yield a peak in their metallicity distributions at about Z_{\odot} . All our default runs overestimate the stellar [O/Fe] ratio, an effect that we demonstrate can be rectified by an increase of the adopted SN type Ia rate. Nevertheless, the models have difficulty in producing stellar metallicity gradients of the same strength as observed in the Milky Way.

Key words: methods: numerical – galaxies: abundances – galaxies: evolution – galaxies: haloes – galaxies: spiral – stars: abundances

1 INTRODUCTION

On large scales, dark matter only cosmological simulations (such as the Millennium runs, Springel et al. 2005; Boylan-Kolchin et al. 2009) have been very successful in reproducing the observed clustering properties of matter in the Universe, and have been of decisive help in establishing the current Λ CDM cosmological paradigm. Numerical simulations have also become an important tool for studying how galaxies in the high-redshift and present-day Universe form and evolve. However, at galactic and sub-galactic scales, the general picture of galaxy formation is still fraught with uncertainty. Much of the current simulation work in the field therefore attempts to clarify the role of different physical processes operating on galactic and sub-galactic scales, as well as their interplay within the cosmological context.

A major difficulty in galaxy formation simulations is the intrinsic multi-scale and multi-physics nature of the problem. In fact, baryonic physics must be properly taken into account in addition to gravity if one wants to obtain a re-

alistic description of galaxy formation and evolution. Unfortunately, important physical processes acting on baryons (e.g. AGN accretion) operate on spatial and temporal scales that are very much smaller than the galaxy as a whole. Nevertheless, these processes play a fundamental role in shaping global galactic features. It is this disparity of scales, together with the uncertainties in our understanding of the baryonic physics involved, that makes galaxy formation such a challenging problem.

To overcome these difficulties, a heuristic parametrization of the most important physical mechanisms for the galaxy formation process is frequently adopted (see Vogelsberger et al. 2013, and references therein). Recently, significant efforts have also been made to develop models that try to self-consistently include more of the relevant physical processes and hence to push back the use of ad hoc prescriptions to ever smaller scales (Hopkins et al. 2011, 2013; Renaud et al. 2013). Treating much of the baryon physics of star formation and associated feedback as ‘subgrid’ is however still the most widely used approach in the field and is inevitable in large cosmological boxes for computational reasons. It has allowed significant advances in our under-

* E-mail: federico.marinacci@h-its.org

standing of galaxy formation by identifying the most relevant physical processes and isolating their role in determining the observed galaxy properties.

In particular, substantial progress has been made on the formation of late-type disc galaxies similar to the Milky Way (Agertz et al. 2011; Brooks et al. 2011; Guedes et al. 2011; Aumer et al. 2013; Stinson et al. 2013; Marinacci et al. 2014). For decades, this has been a sore point in the context of the Λ CDM cosmology because the galaxies predicted by simulations were at odds with what was observationally known. The primary cause of these discrepancies is the so-called *overcooling* problem (Balogh et al. 2001): baryons at the centres of the dark matter haloes that host galaxies cool efficiently through radiative processes on a very short time scale, invariably leading to the formation of overly massive and overly concentrated galaxies (e.g. Abadi et al. 2003; Scannapieco et al. 2008, 2009; Stinson et al. 2010).

Therefore, realistic late-type galaxies can only be formed in simulations when the gas is supplied with an adequate amount of energy capable of partly offsetting its fast cooling rate and curtailing the production of stars. The source of this energy ultimately lies in the back-reaction that the star formation process (and also AGN accretion) exerts on the gas. Several channels (e.g. radiative, thermal, kinetic) are in principle conceivable to couple this energy to the cooling gas, with their relative importance still being debated (e.g. Sales et al. 2014). Different authors agree, however, that the adoption of very strong feedback physics lies at the heart of recent successful simulations of the formation of spiral galaxies (Guedes et al. 2011; Aumer et al. 2013; Stinson et al. 2013; Marinacci et al. 2014).

Independent of the detailed mechanism responsible for the efficient coupling of feedback energy to the star-forming gas, strong stellar feedback is expected to drive galactic-scale winds that expel metal-enriched gas out of the star-forming disc, possibly to distances comparable to or beyond the virial radius of the enclosing dark matter halo. This theoretical expectation appears to be confirmed by observations of star-forming galaxies at high and low redshift, showing that outflows from the sites of star formation to the circumgalactic medium (CGM) are a common phenomenon (Pettini et al. 2000; Strickland & Stevens 2000; Martin et al. 2002; Strickland et al. 2004; Soto et al. 2012).

Simulations suggest that the ejection of metal-enriched gas from galaxies to their haloes via galactic winds has at least two important consequences for galactic evolution. First, the ejected gas is (at least temporarily) unavailable for star formation, thereby preventing its rapid conversion into stars and alleviating the problem of forming overly massive bulge-dominated galaxies. Much of the ejected gas remains however bound to the galaxy’s dark matter halo and thus can be re-accreted, providing fuel for late-time star formation that progressively builds up the disc (Scannapieco et al. 2012).

Second, simulated wind material is in general more metal-rich with respect to the diffuse circumgalactic gas, and therefore represents an important source of metals for this gas component. Besides affecting its chemical composition, the interaction of the wind with the CGM can also significantly alter the dynamical and thermodynamical state of the diffuse gas. As we mentioned above, the mixture of wind material and circumgalactic gas provides fuel for late-

time star formation. Therefore, galactic outflows also have an important influence on the properties of stars (in particular their metallicities), which in turn are responsible for wind generation. Therefore, the properties of the CGM and the metal content of stars comprising the central galaxy offer an important and powerful opportunity to check the consistency of the galaxy formation physics models adopted in numerical simulations.

In this paper we thus aim at investigating how the galactic-scale outflows contained in the simulations of Marinacci et al. (2014, hereafter MPS14) affect the features of the CGM surrounding late-type galaxies and those of the stars that they contain. We use this information as a test of our galaxy formation physics model – in which the galactic wind strength has been primarily set to reproduce the expected stellar mass but *not* the physical state and metal enrichment of the CGM or the detailed metal content of the stellar component – to better understand the limits of our approach, with the goal of using the simulated results to improve its underlying physics description. To this end, we examine the properties of these two components, focusing in particular on their metal content, in a suite of eight hydrodynamical simulations of disc galaxy formation in Milky Way-sized haloes carried out with the moving-mesh code AREPO (Springel 2010). The simulation set has been previously introduced in MPS14, where we analysed the stellar mass distribution of the simulated galaxies, showing that our numerical methodology, which has been designed for applications in large-scale cosmological simulations (Vogelsberger et al. 2014), produces realistic disc galaxies that agree well with the observed scaling relations of late-type systems.

The paper is structured as follows. In Section 2, we summarize the salient characteristics of our simulation set and those of the numerical techniques that we used to perform the runs. We present the results of our analysis in Section 3 separately for gas (Sec. 3.1) and stellar (Sec. 3.2) properties. Finally, we discuss our findings in Section 4 and draw our conclusions in Section 5.

2 THE SIMULATION SET

We analyse a sub-set of the cosmological simulations of disc galaxy formation discussed in MPS14. These simulations can be viewed as hydrodynamical counterparts of the dark matter only simulations carried out in the Aquarius project (Springel et al. 2008), and include eight haloes (labeled Aq-A, Aq-B, etc., until Aq-H) selected to have a final total mass in a small range around $\sim 10^{12} M_{\odot}$, comparable to recent determinations of the mass of the Galaxy (Sakamoto et al. 2003; Battaglia et al. 2005; Dehnen et al. 2006; Xue et al. 2008; Li & White 2008; Boylan-Kolchin et al. 2013). In addition to the mass selection criterion, the Aquarius haloes were chosen to have a relatively quiet merger history by enforcing a moderate isolation criterion, which favours the formation of extended, star-forming discs. More details about the selection criteria and the properties of these haloes can be found in the original Aquarius paper (Springel et al. 2008) and in Boylan-Kolchin et al. (2010).

The Aquarius simulation suite uses the so-called “zoom-in” technique to follow the formation of a target halo with much higher resolution than achievable in a homogeneously

sampled cosmological box. In practice, the Lagrangian region that will collapse to form the central structure is discretized with a high number of low mass particles surrounded by several layers of progressively more massive particles that fill the total simulation volume. The masses of these low-resolution particles increase with distance from the central object, such that the regions further away from the high-resolution volume are sampled more coarsely but still sufficiently well to ensure an accurate accounting of all tidal forces acting on the target halo. This saves computational time without sacrificing the accuracy of the calculation.

In this paper we only analyse a single resolution level which is denoted as level ‘5’, following the naming scheme of the Aquarius project. This also corresponds to the default resolution of the simulations presented in MPS14. The main properties of this resolution level¹ are a characteristic baryonic mass resolution of $\simeq 4.1 \times 10^5 M_\odot$, a dark matter mass resolution of $\simeq 2.2 \times 10^6 M_\odot$ and a maximum gravitational softening length at $z \leq 1$ of 680 pc in physical units for all mass components (dark matter and baryons) in the high-resolution region. In comoving units, the softening length is kept fixed for $z > 1$ in the high-resolution region and its physical counterpart is thus growing until $z = 1$, where it reaches the maximum allowed value and is then held fixed. Common to all the resolution levels in the Aquarius suite are a periodic box of $100 h^{-1} \text{Mpc}$ on a side and a ΛCDM cosmology with parameters $\Omega_m = 0.25$, $\Omega_b = 0.04$, $\Omega_\Lambda = 0.75$, $\sigma_8 = 0.9$, $n_s = 1$ and a Hubble parameter $H_0 = 73 \text{ km s}^{-1} \text{Mpc}^{-1}$ (hence implying $h = 0.73$). This set of cosmological parameters is the same that has been used in the Millennium and Millennium-II simulations (Springel et al. 2005; Boylan-Kolchin et al. 2009) and is consistent with WMAP-1 results. Compared to the more recent Planck findings (Planck collaboration 2013), haloes of given mass in a WMAP-1 cosmology tend to form slightly earlier and hence have on average slightly higher concentration. In $10^{12} M_\odot$ haloes, the increase in the average concentration is $\sim 10 - 20\%$ (see Macciò et al. 2008).

To include gas in the original Aquarius initial conditions, we split each original dark matter particle, regardless of whether it is located in the high- or low-resolution region, into a pair composed of a dark matter particle and a gas cell, so that the whole simulation volume is filled with gas. We note that this differs from many studies performed with the SPH technique (e.g., Stinson et al. 2010; Guedes et al. 2011) where gas is often added to the high-resolution region only, causing a pressure discontinuity at the transition between the high- and low-resolution regions. The mass ratio in each dark matter particle-gas cell pair is set by the cosmic baryon mass fraction, while their positions and velocities are assigned by requiring that the centre-of-mass and the centre-of-mass velocity of the pair are preserved. This is done by displacing the dark matter and cell distributions such that two interleaved particle distributions are formed that are locally shifted relative to each other by half of the original mean inter-particle spacing.

¹ The quoted mass resolution only applies exactly to the Aq-C-5 halo. There are slight differences for the other haloes of the simulation set, within a factor of 2. The detailed list of properties for all the haloes can be found in Table 1 of MPS14.

We evolve the initial conditions with the moving-mesh cosmological code AREPO (Springel 2010). This code solves the gravitational and collision-less dynamics by using the same TreePM approach employed in the popular SPH code GADGET (Springel 2005). For what concerns the hydrodynamic part, AREPO solves Euler’s equations on an unstructured Voronoi mesh by adopting a finite-volume discretization. The flux exchanges between cells are computed via a second-order MUSCL-Hancock scheme (e.g., Toro 1999) coupled to an exact Riemann solver. The special trait of AREPO compared to Eulerian grid-based codes is that the set of points generating its unstructured Voronoi mesh are allowed to freely move, and this additional degree of freedom is usually exploited by moving the mesh-generating points with the local fluid velocity. This causes a transformation of the mesh that adapts itself to the characteristics of the flow, giving rise to a quasi-Lagrangian numerical method which is manifestly Galilean-invariant and keeps the mass of each gas cell approximately constant. Further details about the code structure can be found in Springel (2010), while a detailed comparison between the moving-mesh approach and the smoothed particle hydrodynamics technique is presented in the tests performed by Vogelsberger et al. (2012) and Sijacki et al. (2012). Extensions of the basic method to include ideal magnetohydrodynamics have also been developed (Pakmor & Springel 2013) and applied successfully in cosmological simulations (Pakmor et al. 2014).

The present set of simulations uses a comprehensive model for galaxy formation physics (Vogelsberger et al. 2013) that implements the most important baryonic processes. The model has been specifically developed for the AREPO code and was calibrated to reproduce a small set of key observational findings for the global galaxy population, such as the cosmic star formation history and the galaxy stellar mass function. The full description of the implementation is given in Vogelsberger et al. (2013) to which we also refer for a discussion of the predicted galaxy properties at $z = 0$ (see also Torrey et al. 2014, for an analysis of these properties at high redshift). Among the primary features of the model are:

- (i) primordial and metal cooling rates including self-shielding corrections by Rahmati et al. (2013);
- (ii) a variation of the Springel & Hernquist (2003) sub-resolution model for the ISM with the adoption of a Chabrier (2003) initial mass function;
- (iii) a self-consistent treatment of stellar evolution, mass return from stars and metal enrichment (tracking H, He, C, N, O, Ne, Mg, Si, Fe and total metallicity) of the gas phase;
- (iv) galactic winds implemented via a kinetic wind scheme, with mass loading computed according to an energy-driven scaling (see Puchwein & Springel 2013);
- (v) wind metal loading offset with respect to the mass loading, necessary to reproduce the oxygen abundance of low mass haloes;
- (vi) BH accretion and feedback based on a modification of the Springel et al. (2005) model, accounting for quasar, radio and radiative feedback channels;
- (vii) a spatially uniform UV ionizing background (Faucher-Giguère et al. 2009);
- (viii) a new Monte-Carlo formalism for Lagrangian tracer particles (Genel et al. 2013).

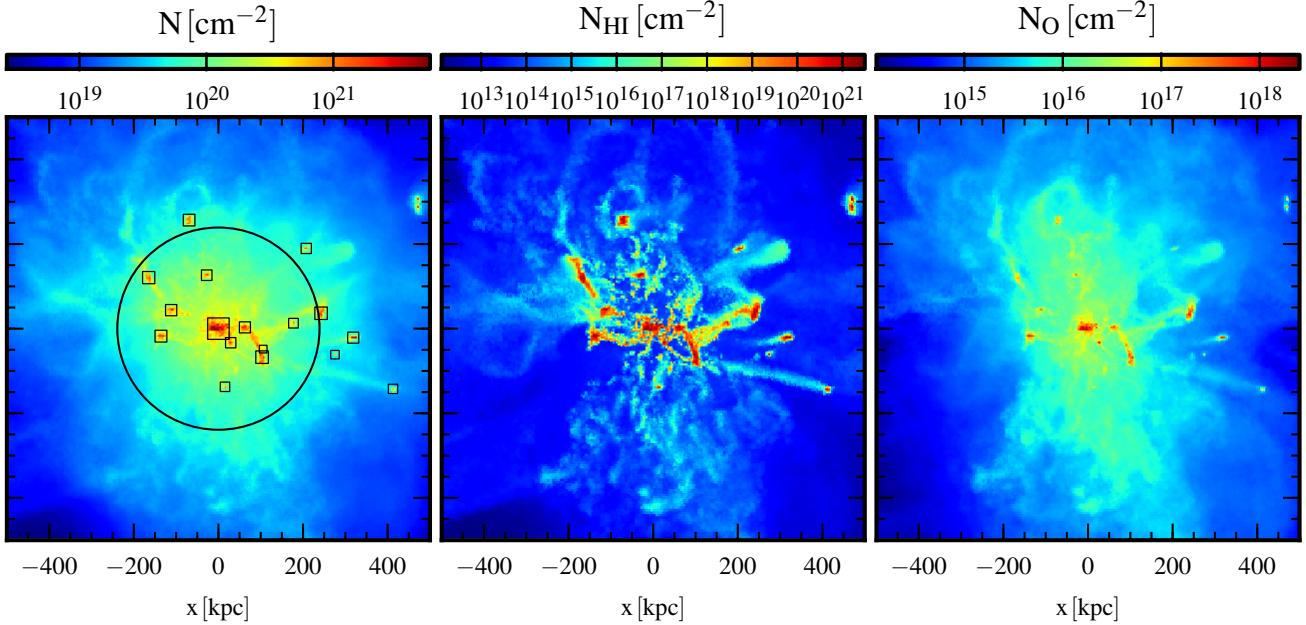


Figure 1. Column density maps of different chemical species for the Aq-A-5 simulation at $z = 0$. To compute the column density only the diffuse gas (i.e., non star-forming gas cells) has been taken into account. In the figure, the halo is oriented such that the central galaxy is seen edge-on to assess the impact of the adopted galactic wind model on the morphology and the metal enrichment of the CGM. To create the maps no cut in systemic velocity has been applied, but only the gas with a distance along the line of sight smaller than 500 kpc relative to the centre of the halo has been considered. In the leftmost panel, the black circle marks the position of the halo virial radius ($R_{\text{vir}} = 239$ kpc), whilst the squares are centred on positions of the main galaxy and of satellites containing gas. Their sizes are scaled according to the gas mass.

We use the same fiducial settings as in Vogelsberger et al. (2013) for the free parameters of the galaxy formation model, except for two minor modifications in the wind implementation and the radio-mode feedback of the BH module, respectively. These modifications are the same as in MPS14 and consist of providing the wind with some thermal energy in addition its kinetic energy, and adopting a more continuous heating model for the radio-mode feedback (see MPS14 for further discussion).

3 RESULTS

3.1 Diffuse gas properties

Before starting the analysis of the features of the diffuse circum-galactic gas, we must define how we select this gas component in the simulations. In the context of our ISM treatment, we consider as diffuse gas all the gas cells whose density is below the star formation density threshold ($n_{\text{th}} \simeq 0.13 \text{ cm}^{-3}$ for the fiducial setting adopted in the simulations). We note that this is a rather broad selection criterion since it encompasses relatively dense ($n \sim 0.1 \text{ cm}^{-3}$) and cold ($T \sim 10^4$ K) gas in the immediate proximity and of the main galaxy (and satellites) as well as more tenuous ($n \sim 10^{-4} \text{ cm}^{-3}$) and hotter ($T \sim T_{\text{vir}}$) gas phase that is expected to be distributed in the CGM on scales of ~ 100 kpc. The properties of the phases comprising this gas component are the topic of this section.

In Fig. 1, we present column density maps at $z = 0$ of the diffuse gas for the case of the simulation Aq-A-5. The

total column density is shown together with the column densities of HI and oxygen to study both the large-scale morphology and the degree of chemical enrichment of the CGM. To create the maps, we choose a projection plane centered on the halo potential minimum, with a size of 1 Mpc on a side. We project all the gas cells that have a distance along the line of sight smaller than 500 kpc from the halo centre. We thus used a purely spatial selection criterion for the projections, although it is also possible to associate the diffuse gas to the halo based on kinematic information (Stinson et al. 2012). The latter method is what is actually adopted in absorption studies of the CGM both in the Milky Way (Sembach et al. 2003; Savage et al. 2003; Lehner et al. 2012) and in external galaxies (e.g., Prochaska et al. 2011) because of the lack of spatial information along the line of sight about the absorbers. However, we explicitly checked that our results do not strongly depend on the way the association between the halo and its CGM is made. For instance, adopting a cut in systemic velocity $|\delta v| = 200 \text{ km s}^{-1}$ produces results nearly indistinguishable from those presented in Fig. 1. Significant differences appear only if a rather extreme cut $|\delta v| < 50 \text{ km s}^{-1}$ is used. In the projections the halo is oriented such that the central galaxy would be seen edge-on. In other words, this means that the vertical axis on the maps is aligned with the galaxy symmetry axis, calculated according to the procedure described in MPS14. We choose that particular orientation because it is the most suited to show the effects of our galactic wind implementation – which is launched preferentially perpendicularly to the disc – on the structure of the CGM.

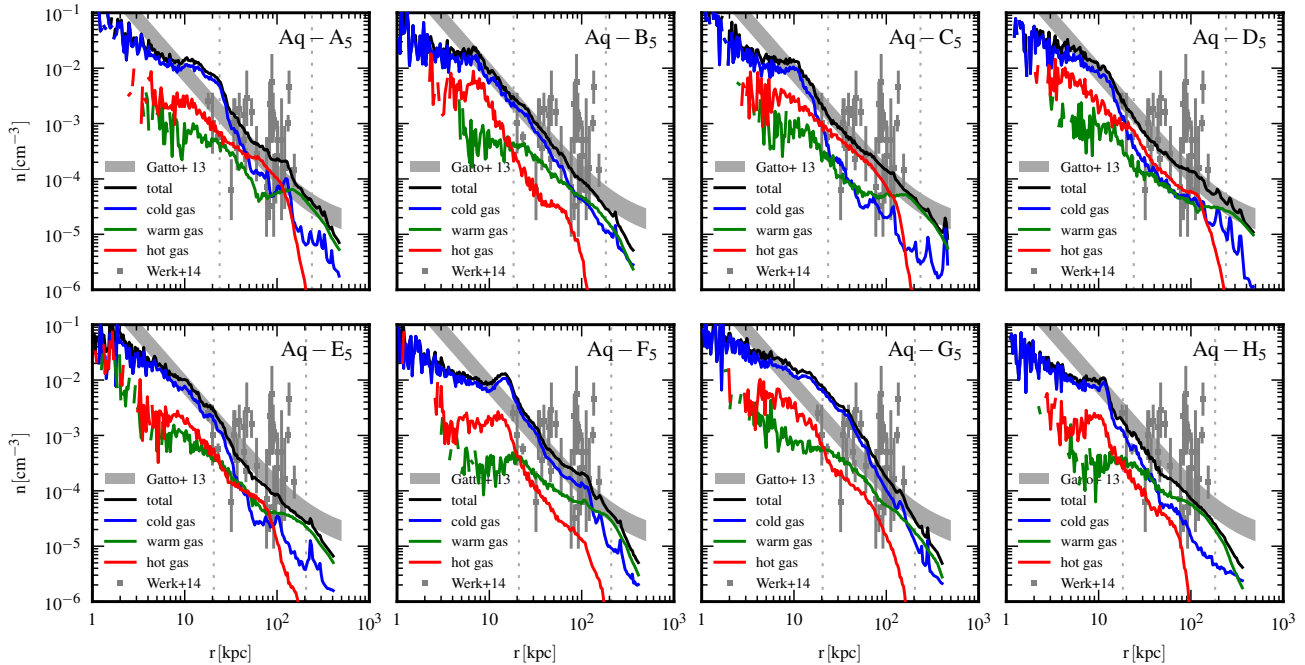


Figure 2. Spherically-averaged density profiles of the diffuse gas as a function of radius for the whole simulation set at $z = 0$. The diffuse gas has been divided into a cold phase (blue line) with $T < 10^5$ K, a warm phase (green line) with 10^5 K $< T < 10^6$ K and a hot phase with $T > 10^6$ K. The total density profile is indicated by the solid black line, while the dotted vertical lines are located at $0.1 \times R_{\text{vir}}$ and R_{vir} , respectively. The gray bands in all panels show the density range of isothermal ($T = 1.8 \times 10^6$ K) models for the Milky Way’s corona derived from ram pressure stripping simulations by Gatto et al. (2013) that take also into account X-ray emission and pulsar dispersion measure upper limits (Anderson & Bregman 2010). Gray points with error bars are taken from Werk et al. (2014) by correcting their hydrogen volume densities for helium and electron abundances (see text for details).

The total column density (left panel) of the CGM exhibits a very regular global morphology and extends in an almost spherical fashion slightly beyond the virial radius of the halo (the black circle in Fig. 1), where a more filamentary structure can be seen. Regions of gas with column densities in excess of 10^{21} cm $^{-2}$ are usually compact and associated with the central galaxy and its satellites (indicated by black squares). This is also confirmed by the HI column density map (central panel), that shows indeed that the vast majority of the high column density gas is accounted for almost completely by this component. The HI morphology is much less regular and less extended with respect to the total column density. The neutral hydrogen tends to be preferentially located close to density peaks (i.e., in the vicinity of the central galaxy and its satellites) and drops by several orders of magnitude in between them. This cold material can be thought of as forming an interface between the star forming region of a galaxy and its environment, possibly mediating further cooling of hotter gas and thus feeding star formation (Marinacci et al. 2010, 2011).

The spatial distribution of heavy elements is similar for all the metal species that we track in our galaxy formation implementation. In the right panel of Fig. 1, we take oxygen as an example. It can be seen that the distribution of this element is markedly different from that of the HI and in fact it resembles more closely that of the total gas. Even in this case oxygen (and the other metals as well) is present up to and also beyond the virial radius of the halo. The presence of oxygen in these regions implies that galactic winds are very effective in ejecting metals from their production sites,

i.e. the star forming regions of the (central) galaxy, to the surrounding environment. The fact that galactic winds are the main agent that causes metal enrichment of the CGM is also indicated by the morphology of the oxygen enriched region. As mentioned above, it looks smoother than the HI distribution and similar to the total gas column density but, compared to the latter, it is more elongated in the vertical direction, which is the preferred direction of wind ejection in our implementation. The wind – which is ultimately powered by supernovae associated with star formation – is more effective in ejecting metal-enriched material in the more active star-forming regions, such as those corresponding to the central galaxy, as can be seen from filaments with column density $\sim 10^{17}$ cm $^{-2}$ emanating from the centre and reaching heights of $\sim 100 - 150$ kpc.

In Fig. 2, we show spherically-averaged density profiles of the diffuse gas as a function of radius for the full simulated set of haloes at $z = 0$. The diffuse gas has been divided into three phases according to its temperature: a cold phase (blue lines) with $T < 10^5$ K, a warm phase (green lines) with 10^5 K $< T < 10^6$ K and a hot phase (red lines) with $T > 10^6$ K. The total gas density is indicated by the solid black line. Each profile has been derived by dividing the radial distance in 100 equally spaced logarithmic bins and then computing the gas mass falling into each bin. The average density then simply follows by dividing the bin mass by the volume of the spherical shell defined by each radial bin. Each halo generally features declining density profiles. The decreasing trend is somewhat less pronounced in the region within $0.1 \times R_{\text{vir}}$, which is marked by the first of the

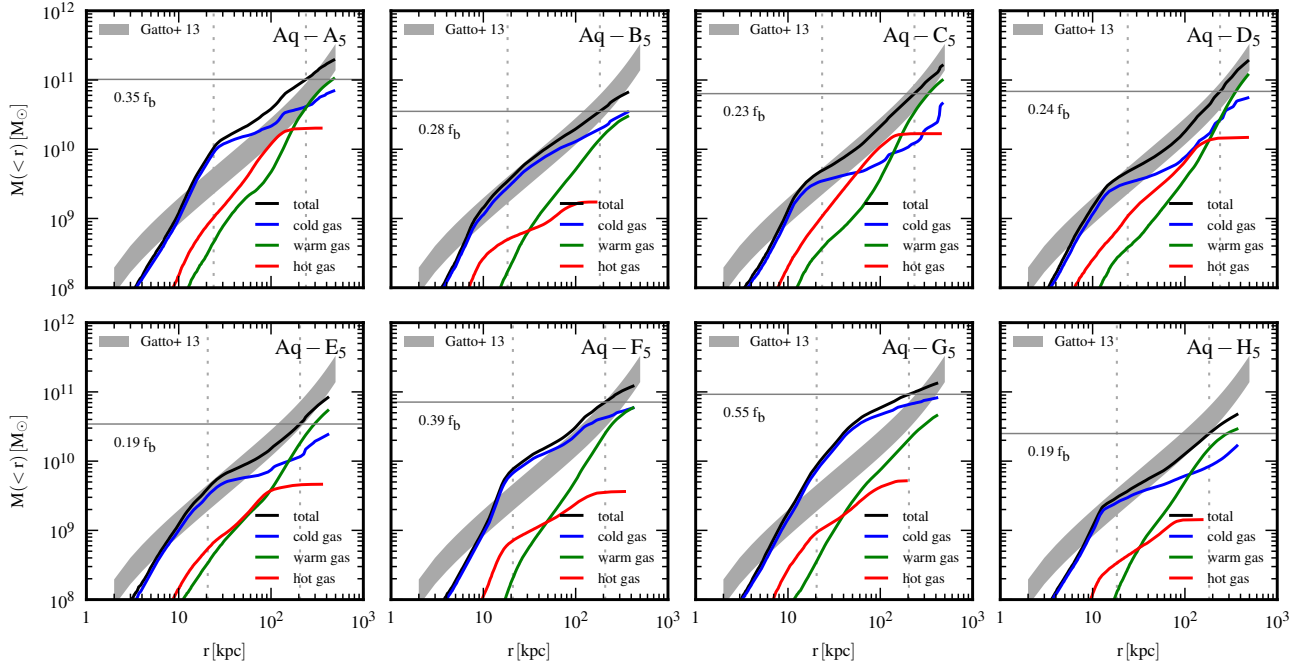


Figure 3. Cumulative mass profiles of the diffuse gas as a function of radius for the whole simulation set at $z = 0$. The contributions to the total mass of different gas phases, separated according to the gas temperature as in Fig. 2, are also plotted. The thin horizontal line in each panel shows the total mass in diffuse gas contained within the virial radius together with the indication of how this mass compares to that inferred from the universal baryon fraction. The gray bands in all panels indicate the allowed range of cumulative mass profiles of the Milky Way’s corona models presented in Fig. 2.

two vertical dotted lines in the Fig. 2 (the other marking the location of the virial radius) and roughly coincides with the extension of the star-forming disc², and then becomes steeper from that point on out to the virial radius. The density profiles are dominated in the inner region by the cold phase. This seems to be the general trend also at larger radii with the noteworthy exceptions of the Aq-A-5 and Aq-C-5 haloes where it is the hot phase that gives the dominant contribution. Some other haloes (Aq-D-5 and Aq-E-5), instead, show a roughly equal contribution to the total density of all three phases.

We compare our density profiles to isothermal models for the Milky Way’s corona of Gatto et al. (2013). These models are derived from ram pressure stripping simulations of the dwarf spheroidal galaxies Sextans and Carina and the allowed density ranges, shown by the gray bands in Fig. 2, take already into account the observational constraints (not reported in the figure) coming from X-ray emission and pulsar rotation measures upper limits in the Milky Way (Anderson & Bregman 2010). The predictions of our simulations are consistent with the admissible density ranges of these models for the Galactic corona. However, we must stress that the match is excellent for our *total* density profiles, while in the simulations of Gatto et al. (2013) the corona is assumed to be composed of hot gas ($T = 1.8 \times 10^6$ K in the models shown here) close to the virial temperature of the Milky Way halo. As we have discussed above, the contribution of the hot gas to our density

profiles is in general sub-dominant with respect to the cold gas. Only in the Aq-A-5 and Aq-C-5 haloes the density of the hot gas phase agrees with the ram pressure stripping constraints derived by Gatto et al. (2013).

We also compare the density profiles obtained in our simulations to COS-Halos data of low-redshift ($z \sim 0.2$) L_* galaxies (Werk et al. 2014) that directly probe the condition of the CGM in late-type systems. To get the total density profiles of the CGM (shown as points with error bars in Fig. 2) we correct the hydrogen density n_H for helium abundance by assuming primordial composition ($X = 0.76$) and for electron abundance by adding to the corrected density $1.16 \times n_H$. The latter value is the mean conversion factor quoted in Fig. 12 of Werk et al. (2014) to obtain their electron density profiles. The predictions of our simulation for the total density profiles of the CGM are in agreement with these observational findings.

Being the dominant phase in terms of density, it is not surprising that most of the mass of the diffuse gas in the simulations is contained in the cold phase. This is shown in Fig. 3, which presents cumulative mass profiles for the three phases defined above. The profiles are computed by ordering the gas cells according to their distance from the halo centre and summing their masses up to a given radius r . The thin horizontal line in each panel represents the total mass in diffuse gas inside the virial radius, and for each system we also report how this quantity compares to the total baryonic mass of the halo as inferred from the universal baryon fraction. Usually, the mass fraction contained in the diffuse gas is not negligible, ranging from $\sim 20\%$ to $\sim 40\%$ of the total baryonic mass in the halo predicted by cosmology, but not dominant either, since only in the case of the Aq-

² We recall that this radial cut was used in MPS14 to select the material belonging to the central galaxy.

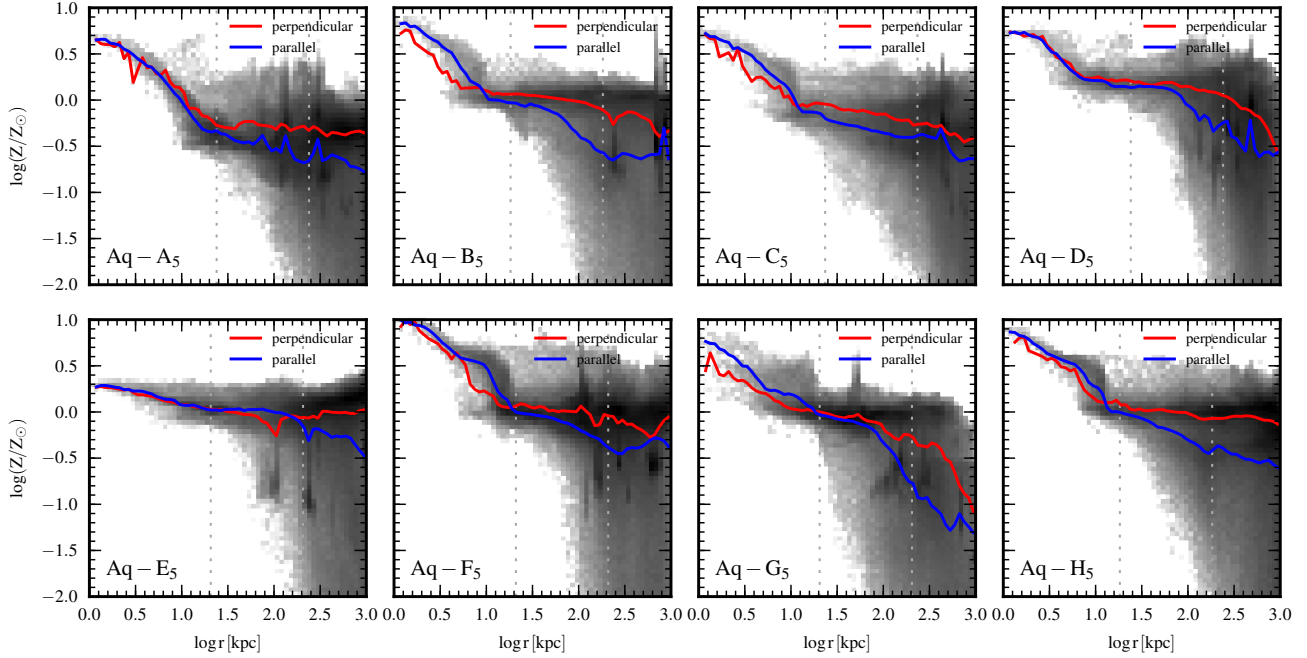


Figure 4. Metallicity distribution versus radial position of the diffuse gas phase for all the simulated haloes at $z = 0$. The figure shows a two-dimensional histogram built on 60×60 equally spaced logarithmic bins and weighted by the mass of gas cells so that the gray-scale encodes the gas mass present in each bin (darker colours indicate larger masses). The red solid lines in each panel represent the (mass-weighted) average gas metallicity as a function of the radius in a cone centered on the symmetry axis of the galaxy with an opening angle of 30 degrees, while the solid blue lines show the same quantity in the region complementary to that cone.

G-5 halo it accounts for about the 55% of the total mass. As mentioned above, most of the mass is contained in the cold phase that shows a rapidly growing profile in the inner 20 kpc (which approximately corresponds to $0.1 \times R_{\text{vir}}$ of the haloes) with a tendency of becoming flatter in the outer regions out to the virial radius. This flattening is always present but can sometimes be more pronounced depending on the relative contribution to the total mass of the warm and hot phases; the most extreme case being the Aq-C-5 halo. For what concerns the (cumulative) mass profiles of the warm and hot phases they present the same trend in the inner regions of the cold counterpart (i.e., a rapid growth) but the mass of the warm gas continues to steadily increase up to the halo virial radius, while the mass of hot gas shows a flattening that is also found in the cold phase. The flatter trend starts at approximately the same radius as that of the cold gas in half of the haloes (Aq-B-5, Aq-F-5, Aq-G-5 and Aq-H-5), while in the others this occurs beyond 100 kpc.

A comparison of our results with those of Gatto et al. (2013) yields again an excellent agreement with respect to the total mass profiles, with values of the enclosed masses within the virial radius that are fairly similar in both cases. It is very encouraging that the two types of simulations reach consistent conclusions for the properties of the circumgalactic gas although they study different phenomena and also differ in the adopted numerical methodology. We stress again that this agreement holds for the *total* mass profile in our simulations, while the Gatto et al. (2013) models describe the hot ($T \sim T_{\text{vir}}$) phase of the circumgalactic gas. Our total CGM masses also provide a good match to the masses inferred by Werk et al. (2014) although their fiducial model predicts that the CGM accounts for $\sim 45\%$ of the

total baryonic mass associated with the $\sim 10^{12} M_{\odot}$ dark matter halo of a typical L_* galaxy, a value close to the upper range of what we find in our simulation set. However, we want to note that CGM mass determinations are very challenging to obtain observationally and highly uncertain. Depending on the assumptions made (especially for what concerns the warm and hot phases of the diffuse gas) the contribution of the CGM to the total baryon fraction can vary by more than a factor of 2 (see Fig. 11 of Werk et al. 2014).

To assess the degree of metal enrichment of the diffuse gas phase as a function of the distance from the central galaxy, we display in Fig. 4 two-dimensional histograms obtained by sampling the $\log Z - \log r$ plane in 60×60 equally spaced bins for all the simulated haloes. The gray-scale encodes the gas mass present in each bin, with darker gray shades indicating larger values of the gas masses. We also show with solid lines two average mass-weighted metallicity profiles obtained by considering two different regions of space surrounding the main galaxy: a cone centred on the galaxy’s symmetry axis (and therefore perpendicular to the star-forming disc) with an opening angle of 30 degrees (red) and the region complementary to that cone (blue). In all the haloes the diffuse gas phase is substantially metal enriched. Inside the central galaxy (i.e. for radii below $0.1 \times R_{\text{vir}}$) maximum metallicities of 3 up to ~ 10 times the solar value are not uncommon. Outside the galaxy, the average gas metallicity shows in general a rather flat trend with radius that in some cases becomes steeper in the proximity of the virial radius. Beyond $0.1 \times R_{\text{vir}}$ the average metallicity in the cone perpendicular to the disc is close to the solar value. The only exceptions are the Aq-A-5, Aq-C-5 and Aq-G-5 systems,

Simulation	r_{\max} (R_{vir})	$M_Z(< r_{\max})$ ($10^{10} M_{\odot}$)	$f_Z(< 0.1 \times R_{\text{vir}})$	$f_Z(< 150 \text{ kpc})$	$f_Z(< R_{\text{vir}})$	$f_b(< R_{\text{vir}})$
Aq-A-5	1.0	0.102	0.514	0.844	1.000	0.55
	2.5	0.161	0.328	0.538	0.637	
	5.0	0.200	0.264	0.433	0.512	
Aq-B-5	1.0	0.111	0.686	0.956	1.000	0.70
	2.5	0.139	0.548	0.764	0.800	
	5.0	0.180	0.425	0.593	0.621	
Aq-C-5	1.0	0.126	0.665	0.863	1.000	0.51
	2.5	0.218	0.386	0.501	0.580	
	5.0	0.258	0.326	0.423	0.490	
Aq-D-5	1.0	0.225	0.635	0.835	1.000	0.68
	2.5	0.372	0.385	0.506	0.606	
	5.0	0.406	0.353	0.464	0.556	
Aq-E-5	1.0	0.098	0.637	0.880	1.000	0.67
	2.5	0.161	0.390	0.538	0.611	
	5.0	0.246	0.255	0.351	0.399	
Aq-F-5	1.0	0.227	0.615	0.922	1.000	0.96
	2.5	0.276	0.507	0.759	0.824	
	5.0	0.311	0.449	0.673	0.730	
Aq-G-5	1.0	0.224	0.513	0.960	1.000	1.03
	2.5	0.244	0.472	0.883	0.920	
	5.0	0.247	0.466	0.872	0.908	
Aq-H-5	1.0	0.116	0.807	0.964	1.000	0.61
	2.5	0.143	0.657	0.785	0.814	
	5.0	0.182	0.514	0.614	0.636	

Table 1. Total metal masses (i.e., including stars and star-forming gas) and metal fractions for all the simulated haloes at $z = 0$. The columns give (from left to right): simulation name; reference radius (in units of the halo virial radius) within which total metal masses are computed; total metal masses (in units of $10^{10} M_{\odot}$); fractions of metals within $0.1 \times R_{\text{vir}}$, 150 kpc and R_{vir} ; and baryon fractions within R_{vir} relative to the cosmological mean.

which feature slightly sub-solar metallicities. The metallicity profiles in the region outside the cone have a somewhat lower value of the metallicity with respect to the region inside the cone and only in the case of the Aq-E-5 halo the two profiles agree. This trend is either inverted or the two profiles have essentially the same metallicity values inside the central galaxy.

The presence of a significant degree of metal enrichment in the haloes of our simulated galaxies demonstrates again the effectiveness of galactic winds in transferring metals from their production sites (the star-forming discs) to the circumgalactic regions surrounding them. Moreover, the scatter in the metallicity distribution tends to increase with radius. This implies that at any given radius, regions with rather different metallicity co-exist or, in other words, that metals are not homogeneously mixed in the gas. The bipolar nature of our galactic wind model (see also the right panel of Fig. 1) spontaneously leads to this type of behaviour because of its intrinsic anisotropy, which is also the cause for the differences between the metallicity profiles perpendicular and parallel to the disc discussed above.

To further characterize the degree of metal enrichment of the CGM, in Table 1 we present the total metal masses and metal fractions for all the simulated haloes at $z = 0$. Note that all the entries in the table include also the contributions of stars and star-forming gas to properly account for all the metal content of the simulated haloes. These components, however, only contribute to the metal content of the central galaxy, where they are located. We list the total metal masses within three different fiducial radii (namely

1.0, 2.5 and 5.0 times R_{vir}) and the corresponding metal fractions within $0.1 R_{\text{vir}}$, 150 kpc (the reference radius in Peeples et al. 2014) and R_{vir} . Finally, in the last column we report the baryon fractions within the virial radius taken from MPS14.

Metal masses steadily increase as the fiducial radius increases, implying that a non-negligible fraction metals is located beyond the virial radius of all the simulated systems. For a reference radius of $2.5 \times R_{\text{vir}}$ this fraction can be as high as 40% of the total metal mass. At the same fiducial radius, the metal fractions within 150 kpc are in the range $\sim 50 - 80\%$ of the total metal masses. While the lower value of this range it is still consistent with that presented by Peeples et al. (2014), who report that for a typical L_* galaxy only $\sim 40\%$ of the total metal mass should be found inside 150 kpc, about half of our objects have metal fractions close to 80%. Interestingly, higher baryon fractions appear to correspond to higher metal fractions, although this correlation is not particularly strong. Most of the metals in the haloes are found within $0.1 \times R_{\text{vir}}$ – the adopted size of the central galaxy – and are contained in stars and star-forming gas. This component accounts for more than 50% of the metal mass contained within 150 kpc for all the haloes.

In Fig. 5 we present the phase diagram of the diffuse gas for all the simulated haloes at $z = 0$. Specifically, we built a two-dimensional histogram by dividing the $\log T - \log n$ plane in 80×120 equally spaced bins and plotting, as a grayscale, the total gas mass inside each bin (darker gray shades are assigned to larger values of the mass). From Fig. 5, it is clear that the diffuse medium it is not uniformly distributed

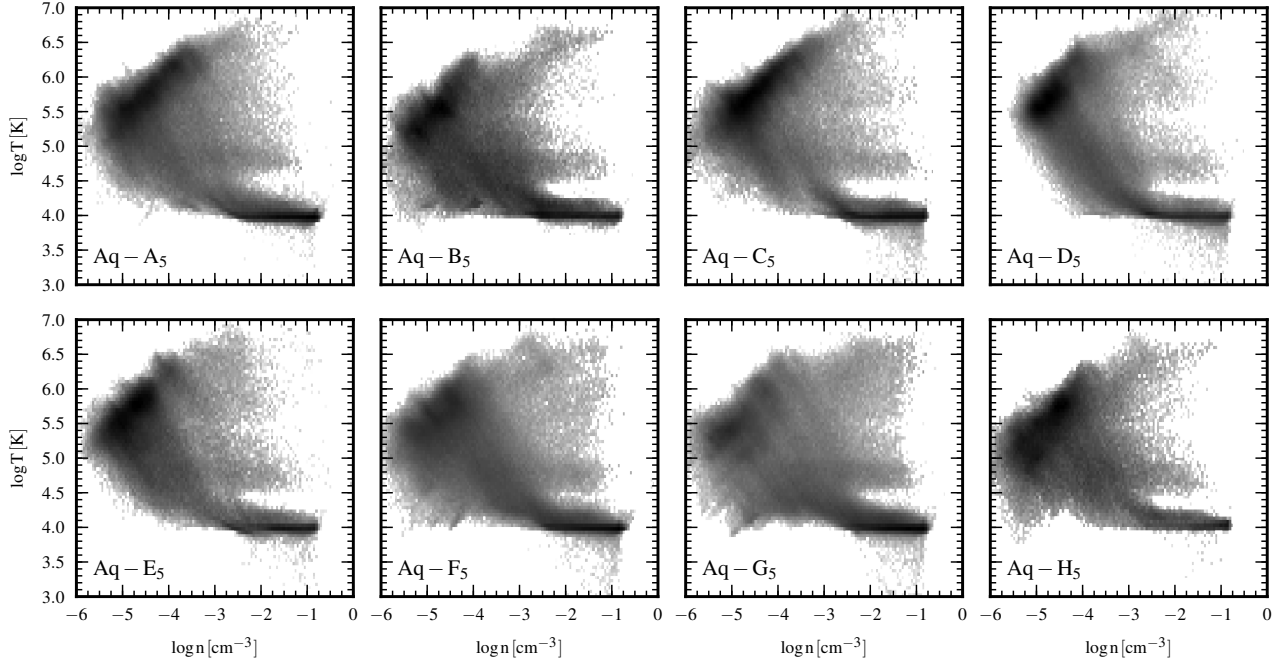


Figure 5. Phase diagram of the diffuse gas phase for all the simulated haloes at $z = 0$. The $\log T - \log n$ plane is divided in 80×120 equally spaced bins on which a two-dimensional histogram is built. The histogram is weighted by the gas mass present in each cell and the gray-scale encodes the amount of mass present in each bin (darker colours indicate larger values of the mass). It is readily apparent that the diffuse medium tends to concentrate in two distinct parts of these diagrams, one located towards high densities ($10^{-2} \text{cm}^{-3} < n \lesssim 1 \text{cm}^{-3}$) and low temperatures ($T \sim 10^4 \text{K}$), and the other at low densities ($10^{-5} \text{cm}^{-3} < n < 10^{-3} \text{cm}^{-3}$) and temperatures close to the virial one ($\sim 10^6 \text{K}$).

in the $\log T - \log n$ plane but gathers in two definite regions of the diagrams. One region is located at low densities ($10^{-5} \text{cm}^{-3} < n < 10^{-3} \text{cm}^{-3}$) and at temperatures $\log T \gtrsim 5.5$ and centred on the halo virial temperature, which for the halo mass range that have been explored in these simulations is $\sim 10^6 \text{K}$. This warm-hot gas may be identified with the extended component of the CGM seen in the left and right panels of Fig. 1. The other region is at higher densities ($10^{-2} \text{cm}^{-3} < n \lesssim 1 \text{cm}^{-3}$) and at an almost constant temperature of 10^4K . This cold and relatively dense gas is closely related to the HI map presented in the central panel of Fig. 1 from which it can again be seen that this gas is found in the proximity of the central galaxy and its satellites and therefore has a less extended spatial distribution with respect to the warm-hot component. The transition between these two gas phases is not sharp but rather continuous. Indeed, the remaining part of the diagram in between the warm-hot and the cold dense gas is populated by an intermediate gas phase that can either result from the cooling of the denser and hotter fraction of the warm-hot phase via radiative losses – the less dense fraction can have a cooling time comparable or longer than a Hubble time – or the heating of the cold phase by the thermalization of the galactic wind energy or AGN feedback.

To quantify how the energy injected by the wind into the CGM affects the thermodynamic state of the latter, we show in Fig. 6 the spherically-averaged differential luminosity profiles of the diffuse gas together with the energy produced by stellar feedback that is available for galactic winds. Again, we split the contribution to the total gas luminosity

between its cold, warm and hot phases. We derived the luminosity profiles by computing the total cooling rate of the gas (and thus the luminosities that we plot are *bolometric* luminosities) in 35 equally spaced logarithmic radial bins and then dividing the resulting rate by the bin width. The energy available to galactic winds is estimated by adding up the star formation rate (SFR) of star-forming gas cells within a given bin. This quantity is then converted into an energy rate by using a factor that expresses the supernova energy per unit mass for a Chabrier (2003) initial mass function times the assumed wind efficiency factor (for details see Vogelsberger et al. 2013, section 2.5.1). Also in this case the radial profile is obtained by dividing the supernova energy rate thus computed by the bin width.

Several important aspects can be appreciated from Fig. 6. Perhaps the most important one is that the energy in the galactic winds, that in our model contain nearly all the energy originating from supernovae, can easily compensate for the radiative losses of the gas. This immediately suggests that the wind energy is one of the major energy sources of the diffuse medium, if not the most prominent. Most of the wind energy is generated within the inner $\sim 20 \text{kpc}$ of the haloes (roughly the size of the star-forming region), where the central galaxy is located and star formation is more vigorous. In this region, the supernova energy available to winds is comparable and in several cases even offsets the radiative losses of the gas, the only exception being the Aq-E-5 halo. Indeed, this object has the lowest SFR at redshift $z = 0$ of the whole simulation set (see Fig. 14 of MPS14), which implies a lower supernova rate and hence less energy avail-

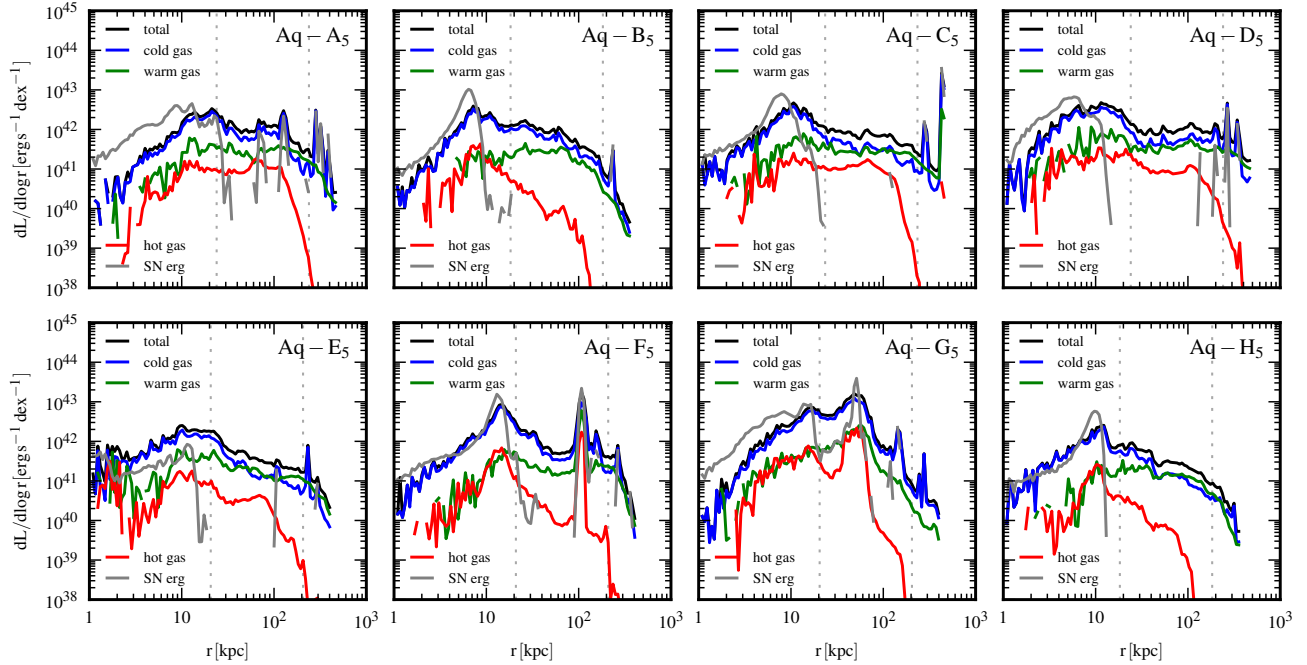


Figure 6. Spherically-averaged differential (bolometric) luminosity profiles for the diffuse gas phase for all the simulated haloes at $z = 0$, computed as the total cooling rate in equally logarithmically spaced radial bins divided by the bin width. The relative contributions of the cold, warm and hot components, selected according to the the gas temperature (see also Figs 2 and 3 above), are shown together with the energy of supernovae (gray lines) that is contained in galactic winds and ultimately deposited in the CGM of the simulated galaxies. Peaks in the latter quantity are usually found at the same locations of those of the total gas luminosity, suggesting that the energy carried by galactic winds is one of the major factors which sets the thermal state of the diffuse gas.

able to generate galactic winds. The energy produced in the central regions is transferred to the CGM through the interaction between galactic winds and the CGM itself. This interaction eventually leads to the thermalization of the wind energy, which is thus available for powering the emission of the circum-galactic gas. The supernova rate suddenly drops at radii greater than ~ 20 kpc and so obviously does the wind energy, although occasional peaks of this quantity, very likely due to the presence of star-forming satellites, can be observed in the external regions. The presence of these peaks is very interesting because they are always accompanied by a corresponding peak in the gas luminosity. This further reinforces the idea that galactic winds are an important energy input sustaining the gas radiative losses.

Another key point is the fact that almost all of the gas luminosity is accounted for by the cold phase up to distances of ~ 100 kpc, where usually the warm phase gives a similar contribution. The hot phase is always sub-dominant in the luminosity budget. This is not surprising because gas in the cold and warm phases have temperatures that encompass the range where cooling is enhanced by the presence of metals (for solar metallicity, the cooling function peaks at a few $\times 10^5$ K). Furthermore, in the cold phase the enhancement due to the presence of metals is further assisted by a greater gas density. The hot phase lacks both of these boost factors: it has sufficiently high temperature to be located away from the peak of the cooling function – and actually at temperatures of $\sim 10^6$ K it is close to a *local minimum* of the cooling function before the cooling rate starts to increase again due to free-free emission – and its density is low, rarely exceeding a few 10^{-3} cm^{-3} and only in innermost regions (see Fig. 2).

3.2 Stellar metallicities

We now pass to analyse the metal content of stars comprising the central galaxy in our simulations to see how this is affected by strong galactic outflows. We first focus on the global metal content (Sec. 3.2.1) and we then discuss how the metal abundance varies as a function of the galactocentric radius (Sec. 3.2.2).

3.2.1 Global metallicity distribution

We start our analysis of stellar metallicity by presenting first its global distribution. We will focus on stars belonging to the central galaxy adopting our usual spatial cut that includes only stars inside $0.1 \times R_{\text{vir}}$ of the host halo. Since the virial radii of all the simulated objects are ≈ 200 kpc, this spatial cut will include disc and bulge stars, as well as so-called halo stars (i.e., stars outside the disc of the central galaxy and gravitationally bound to it).

In Fig. 7, we show histograms of the iron distribution – a widely used proxy for the total metal content – relative to the solar value (taken from table 5 of Asplund et al. 2009) of such stars for all the simulated objects at $z = 0$. The histograms are normalised to the total stellar mass, and the contributions of disc (blue area) and bulge (red area) stars are also displayed. To separate these contributions we adopted the same kinematic criterion as in MPS14 based on the circularity parameter ϵ of stellar orbits, so that stars with $\epsilon > 0.7$ are considered as being part of a rotationally supported disc while the remaining part comprises the bulge. The total iron distribution has a peak at $[\text{Fe}/\text{H}] \sim 0$ in al-

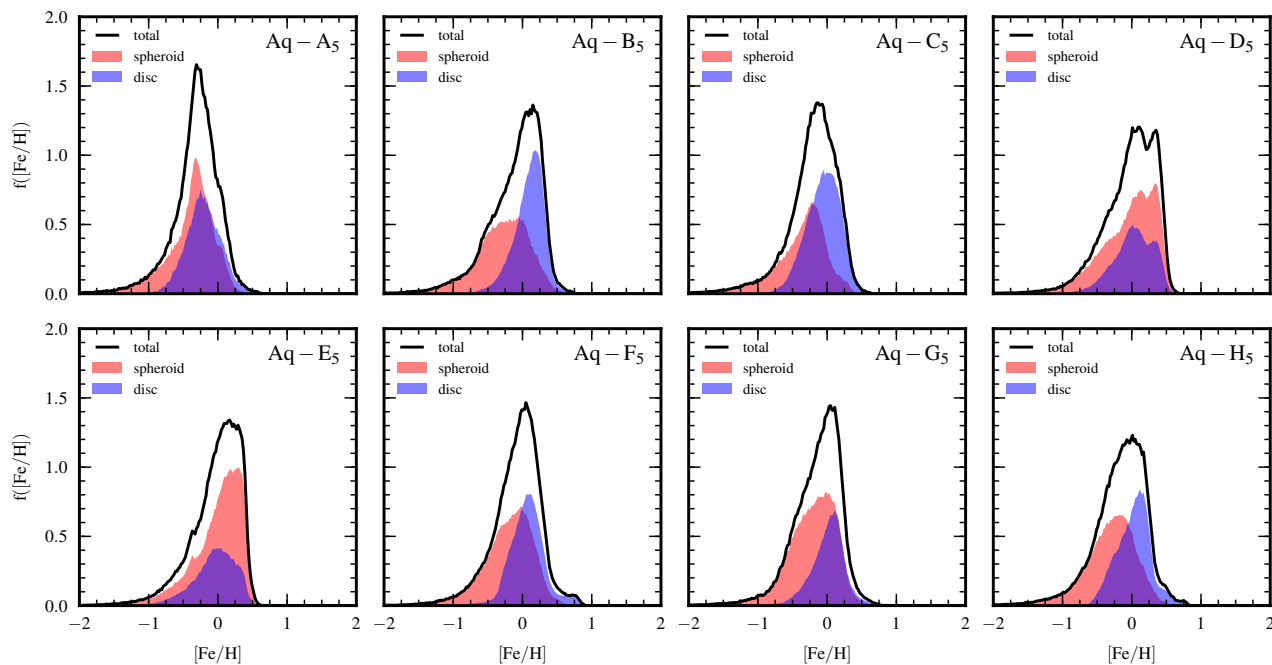


Figure 7. Histograms of the iron abundance relative to the solar value of stars within $0.1 \times R_{\text{vir}}$ for all the simulated haloes at $z = 0$. The contributions of disc and bulge stars, separated according to their circularity parameter ϵ , are also shown. The histograms are normalized such that the area below them represents the stellar mass fraction in each component. Most of the histograms present a distribution of stellar metallicities peaked at around $[\text{Fe}/\text{H}] \sim 0$ and skewed towards sub-solar values. This general behaviour results from the superposition of the contributions of disc stars that are on average more metal-rich (because they are younger) and more narrowly distributed around the location of the peak of their metallicity distribution, and less metal-rich bulge stars that have a broader distribution with a tail towards lower metallicities.

most all the haloes. The only exception is Aq-A-5, where the peak of the distribution is shifted towards lower metallicities, giving $[\text{Fe}/\text{H}] \sim -0.8$. Usually, the iron distributions are unimodal and rather symmetric around their maximum value, although with a tail at sub-solar metallicities. Occasionally a second peak, as in the case of the Aq-D-5 halo, or a small bump at super-solar metallicities, for instance in the Aq-F-5 and Aq-H-5 haloes, may be present.

The features of the total metallicity distributions are the result of the superposition of the distributions of disc and bulge stars that have quite different properties. Both distributions are unimodal (except again those of Aq-D-5) but they usually peak at different metallicities. For disc stars the peak is located at solar or slightly super-solar metallicities, while bulge stars are less metal-enriched and the peak of their distributions is located at sub-solar values. This is not surprising because the iron abundance (total metallicity) is a good tracer of the stellar age. Since disc stars are on average younger than bulge stars in this set of simulations (see MPS14), they form from a more metal-enriched interstellar medium, while older bulge stars are composed from more pristine material. However, not all the haloes feature peaks at two different locations. In particular, there are two exceptions, namely haloes Aq-D-5 and Aq-E-5, where the metallicities of disc and bulge stars are very similar. It is interesting to notice that these two exceptions are also the two most bulge-dominated galaxies of our whole simulation set. Another distinctive difference between the metallicity histograms of disc and bulge stars is that the former are more narrowly distributed around their peak value, whilst

the latter have a broader distribution and a significant tail at lower metallicities which is absent for disc stars. Due to the narrowness of the distribution, and also to the fact that most of these systems are disc-dominated, the peak of the distribution is usually more prominent for disc stars.

In Fig. 8, we present two-dimensional histograms of the $[\text{O}/\text{Fe}]$ abundance versus the $[\text{Fe}/\text{H}]$ abundance at $z = 0$ for all the simulated haloes. The histograms are generated by dividing the $[\text{O}/\text{Fe}] - [\text{Fe}/\text{H}]$ plane into 80×300 equally spaced bins and computing the stellar mass falling into each bin. This quantity is encoded by the gray scale in Fig. 8, with darker gray shades assigned to larger masses. From stellar evolution theory an anti-correlation between the two abundances is expected. The strength of the anti-correlation (i.e., the slope in the diagram) is of course influenced by the details of the star formation history of the galaxy, but its origin lies mainly in the channels that are responsible for the production of oxygen (and the so-called α elements of which oxygen is the most abundant) and iron. Oxygen is mostly produced in core-collapse supernovae generated by the explosion of massive stars ($> 8 M_{\odot}$), while the main channel for iron production is represented by type Ia supernovae – thermonuclear explosions of white dwarfs. Because of the mass difference in the progenitors of these classes of objects, their explosion times are very different. In particular, core-collapse supernovae explode promptly, enriching the ISM rapidly with α elements, while type Ia supernovae need more time before they can start the iron enrichment. This implies that younger stars, that form from a more type Ia-enriched ISM and thus contain more iron, will have on av-

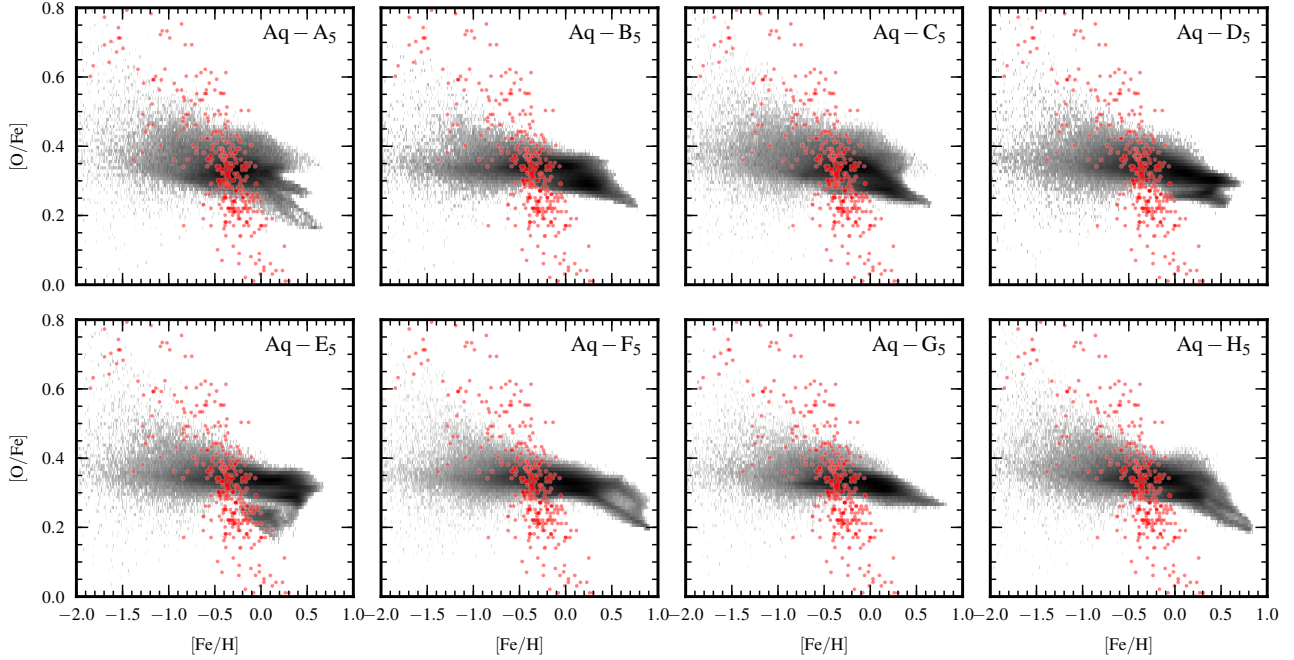


Figure 8. Oxygen versus iron abundance of stars within $0.1 \times R_{\text{vir}}$ for all the simulated haloes at $z = 0$. The $[\text{O}/\text{Fe}] - [\text{Fe}/\text{H}]$ plane is divided in 80×300 equally spaced bins on which a two-dimensional histogram is built. The histogram is weighted by the star particle mass and the gray-scale encodes the stellar mass present in each bin (darker colours indicate larger masses). In the $[\text{O}/\text{Fe}] - [\text{Fe}/\text{H}]$ plane stars form a sequence that for increasing values of the iron abundance shows a slowly decreasing trend in the $[\text{O}/\text{Fe}]$ values, although a substantial scatter is present. However, when compared to Milky Way data (red points) the trend is much flatter than the observed one. Especially at $[\text{Fe}/\text{H}] \sim 0$ our results are unable to reproduce the sharp cut-off in the $[\text{O}/\text{Fe}]$ abundances present in the data.

erage a small $[\text{O}/\text{Fe}]$ ratio since there has been enough time for type Ia supernovae to efficiently enhance the abundance of iron with respect to the α elements. Given its origin, reproducing this anti-correlation is therefore an important test for the stellar evolution model and metal enrichment scheme employed in our simulation set.

From Fig. 8 it can be seen that at low metallicity (low values of $[\text{Fe}/\text{H}]$) there is significant scatter in the histograms, but this is reduced at higher metallicities ($[\text{Fe}/\text{H}] > -0.5$) where a well-defined sequence forms in all the panels. Most of the times the sequence is not unimodal but there is a hint of a gap located at $[\text{O}/\text{Fe}] \sim 0.3$. The declining trend of $[\text{O}/\text{Fe}]$ with $[\text{Fe}/\text{H}]$ is present in all the panels, but it is never very pronounced and tends to steepen, sometimes considerably, with increasing metallicity. Interestingly, in two of the haloes that show a double sequence, namely the Aq-B-5 and the Aq-C-5 haloes, the sequence with the higher value of $[\text{O}/\text{Fe}]$ seems to show an inversion of the relation. A comparison with Milky Way data (red points) for halo, thick disc and thin disc stars³ reveals, however, that the observed anti-correlation is much steeper than that present in our simulations. In particular, the oxygen abundance predicted by the simulations matches the observed values only in a narrow range of iron abundance between -0.5 and 0 . At lower metallicities, some isolated histogram bins can reproduce the observed $[\text{O}/\text{Fe}]$ ratios of the most metal-poor stars – we recall that data points are individual stellar measurements –

but the bulk of the distribution has an oxygen abundance ~ 0.3 dex below the observed values. The disagreement is about a factor of 2 and it may just be an indication of the uncertainties in the elemental yields that we adopted for low metallicity stars. We also note that, as far as the lower metallicity part of the panels is concerned, other simulations reach similar results (see e.g. Gibson et al. 2013). At higher metallicities, the discrepancy is more marked and our results are not able to capture the sharp cut-off in oxygen abundance observed at $[\text{Fe}/\text{H}] \sim 0$. The likely cause of this behaviour is either a slight over-production of oxygen in our simulations or an underproduction of iron due to a too low SNIa rate at late times, a question we further examine in Sec. 4.

3.2.2 Radial metallicity gradients

Since in the simulations the metallicity information of stars is available together with their positions, it is interesting to investigate how the (average) metallicity of the stellar component varies as a function of position. In particular, several observational surveys of the Milky Way disc (see Rudolph et al. 2006; Coşkunoğlu et al. 2012, and references therein) and of external spiral galaxies (e.g., Sanders et al. 2010; Barker et al. 2007; Magrini et al. 2009) report that the amount of metals is a decreasing function of the galactocentric distance of stars. It is therefore important to compare the predictions of our simulations with this observational fact.

We do this for the oxygen abundance in Fig. 9, where

³ Observational data is a compilation from Gratton et al. (2003), Reddy et al. (2003), Bensby et al. (2005) and Ramya et al. (2012).

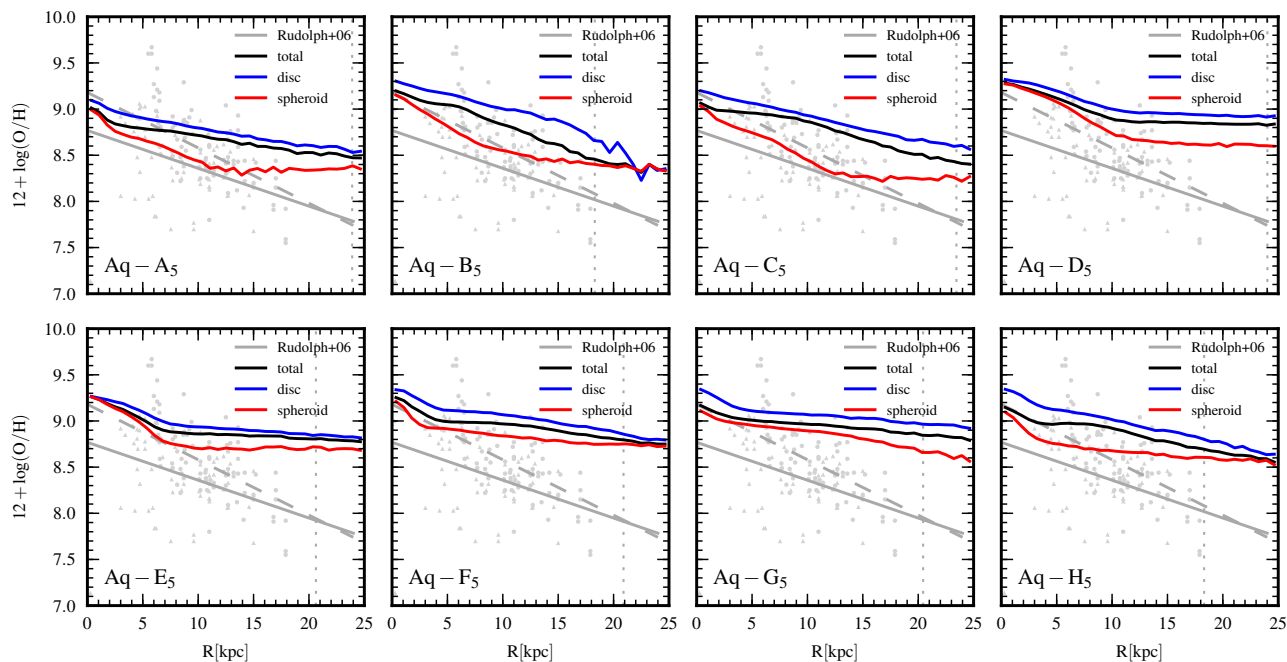


Figure 9. Stellar oxygen abundance as a function of galactocentric radius of star particles with $R < 25$ kpc and $|z| < 0.1 \times R_{\text{vir}}$ for all the simulated haloes at $z = 0$. The plots show the radial abundance profiles in three different cases: the total sample of stars (black lines), the disc stars (blue lines) and bulge stars (red lines). Gray points are Milky Way data taken from Rudolph et al. (2006) with gray lines representing two different fits of the data in the case of IR derived metallicities (solid lines) or optical derived metallicities (long-dashed lines). The vertical dotted lines are located at $0.1 \times R_{\text{vir}}$. The oxygen abundances predicted by the simulations are in agreement with the observed values and a metallicity gradient is clearly visible in all the panels for all the considered components, although it is always too shallow when compared to the observations.

we present the average abundance profile of oxygen as a function of the galactocentric radius R for all the simulated haloes at $z = 0$. The abundance profile is derived by subdividing the radial range in 35 equally spaced bins and then by computing the total oxygen mass of the stars within a given bin divided by the total stellar mass in that bin. To use the same radial extent in all the panels, we have somewhat modified the spatial selection criterion for the stars, which are now included in the calculation only if they are inside a cylinder of radius 25 kpc that extends above and below the plane of the galactic disc for $0.1 \times R_{\text{vir}}$. This distance is indicated in all the panels by the vertical gray dotted line. We also show, as gray points, the observed metallicities of 117 Galactic H II regions taken from Rudolph et al. (2006) together with two best-fitting relations derived by considering the sub-sample of sources whose metallicities are estimated through IR observations (solid gray line) or optical observations (long-dashed gray line). We recall that H II regions are kept ionised by the radiation of very young stars located at their centres, and therefore their metallicity is a reliable indicator of the metal content of the stars at their interior. In Fig. 9, we separately present the oxygen profiles for the total sample (black line), the disc (blue), and the bulge (red) stars. The separation in bulge and disc stars is performed based on the same criterion adopted in section 3.2.1.

By inspecting Fig. 9, one can immediately see that the oxygen abundance generally declines as a function of galactocentric radius in all the haloes. In agreement with the findings of Fig. 7, disc stars have an oxygen content always larger with respect to bulge stars. Since these plots show ba-

sically a mass-weighted metallicity, the oxygen abundance of the total sample lies in between the values for disc and bulge stars. Another important aspect is that the predicted values of the stellar oxygen abundance are compatible with the observations although, if one focuses on the total sample and on disc stars, it is at the upper end of what it is currently observed, especially at large galactocentric radii. This is presumably linked to the high $[\text{O}/\text{Fe}]$ values at high stellar metallicities that have been discussed in Fig. 8 and again suggests that in our simulations the amount of oxygen may be mildly overproduced.

We noted earlier that the oxygen profiles are declining with radius; thus a metallicity gradient is present. For what concerns its strength, it is apparent from the comparison with the two best-fitting relations that in general the gradients predicted by our simulations are too shallow, even considering the optical fit to the data which has the least pronounced slope. Only in two cases (Aq-B-5 and Aq-C-5) the slope of the optical best-fitting relation is reproduced, but there is a considerable offset toward higher abundances, as previously discussed. In some of the haloes (Aq-A-5, Aq-B-5 and Aq-C-5), bulge stars do a considerably better job in capturing the predicted metallicity trend, both in slope and normalisation.

We must caution the reader that H II regions surround newly formed stars in the Galactic disc and as such are associated to a very young stellar population and the most metal rich gas. In our comparison we did not use any age cut for the stars, thereby including also old and metal poor stars. This in principle could affect our conclusions. However, we

have explicitly checked that even restricting the comparison data to the youngest stars (age < 300 Myr) does not influence our results significantly. In some cases (Aq-A-5, Aq-B-5 and Aq-C-5) this may lead to a steepening of the metallicity profile, but a too flat stellar metallicity gradient is still present in the majority of the simulated galaxies.

4 DISCUSSION

In the previous sections we have presented the main properties of the diffuse gas and stellar metallicity distributions that our simulations predict for galaxies similar to our own Milky Way. Here we extend the discussion on how these results compare to observations, examining in more detail which observational constraints are matched and where tensions between our simulations and the data lie.

We start with the properties of the diffuse gas surrounding the main galaxy. The picture that emerges from the simulations is that the structure of this gas component is strongly affected by galactic-scale winds, which in our simulations are necessary to curtail star formation. This is particularly evident if one compares the bipolar morphology (caused by the fact that the galactic wind is preferentially ejected perpendicularly to the star-forming disc in our current implementation) in the column density map of metals to the global morphology of the gas (see Fig. 1). The same comparison also shows that the diffuse gas is significantly metal enriched out to and beyond the virial radius, and Fig. 4 backs up this conclusion. The average metal content in the diffuse gas is a slowly declining function of radius and, although a significant scatter is present, the average gas metallicity is close to solar. This value is larger than that commonly inferred from observational constraints in the Milky Way other nearby galaxies, which seem to prefer a value closer to $\sim 0.1 Z_{\odot}$ (Hodges-Kluck & Bregman 2013; Miller & Bregman 2013). However, due to its very low density, the metallicity of the diffuse gas phase and especially that of the hot emitting X-ray gas is poorly constrained. This metallicity is hence often simply either assumed or allowed to vary between $0.1 - 1 Z_{\odot}$ (Anderson et al. 2013).

There is also another crucial factor that can substantially impact the degree to which the halo gas is enriched by metals. In our wind model, the metal loading of the wind can in principle be chosen *independently* from its mass loading. This was introduced to accommodate the fact that the mass loading is expected to arise in part through entrainment of gas with much lower metallicity than that of the star-forming gas itself. Indeed, it proved necessary in our wind model to allow galaxies to retain enough metals such that the observational relation between their stellar masses and metal content (see Fig. 13 in Vogelsberger et al. 2013) could be matched, while still efficiently expelling baryons to control star formation. The standard choice for our wind model is to load the outflow only with 40% of the metal mass contained in the parent gas cell, while the remaining part is redistributed to the neighbouring ISM particles. The results presented here suggest that even with this reduced metal loading our galactic winds are able to significantly enrich the CGM with metals and to eject an appreciable fraction of the total metal mass beyond the virial radius of the enclosing halo (see also Table 1). Within 150 kpc our

simulated haloes contain 50-80% of their total metal budget. Half of the sample is close to the upper boundary of this range, which is a factor of ~ 2 higher than what found in COS-Halos data (Peeples et al. 2014).

Although the distribution of metals in the halo is in tension with what is observationally known, other properties of the diffuse gas such as density and mass distributions match Milky Way and other late-type galaxies constraints quite well. The mass contained in the diffuse gas component is a substantial fraction of the total baryonic content of the halo (up to $\simeq 50\%$ of the universal baryon fraction), but in general the haloes are not baryonically closed (see last column of Table 1). The total densities are consistent with those determined at low redshift for L_* galaxies (Werk et al. 2014). They are also compatible with the densities needed to strip gas via ram pressure from dwarf spheroidal galaxies in the Milky Way (Gatto et al. 2013). However, we must note that the simulations in Gatto et al. (2013) were primarily aimed at investigating the hot phase of the diffuse CGM (the so-called hot corona). We caution again that this phase is somewhat underrepresented in our simulations, except in haloes Aq-A-5 and Aq-C-5.

The stellar metallicities in our simulations are able to capture the general trends expected in the Galaxy. For instance, the stellar iron content shows that disc stars are more metal rich and younger with respect to their bulge counterpart and the iron distribution peaks roughly at the solar value. However, when simulations are compared in more detail to the observations, discrepancies start to emerge. We note that in our model the processes for the injection of metals into the ISM and for the ejection metals through wind particles are related, but are not explicitly coupled as is frequently done in feedback models that inject metals concurrently and into the same gas as the energy that is intended to drive winds (e.g. Agertz et al. 2011; Guedes et al. 2011; Aumer et al. 2013; Simpson et al. 2013; Stinson et al. 2013). Therefore, the fidelity of our simulated stellar metallicities with observations does not necessarily constrain the previously described results for the properties of the CGM.

A significant discrepancy for stellar metallicities is that our simulations have only a very weak dependence of the [O/Fe] abundance with respect to [Fe/H]. This relation is an important indicator of the relative contribution of core-collapse versus type Ia supernovae to metal enrichment. As such, it represents an important test of our stellar evolution module. In addition to the details of the star formation history in each halo, there are two major factors that can influence the [O/Fe]-[Fe/H] relation. The first is due to the uncertainties in the metal yields that we adopted in the model, which can induce an over- or under-production of one or several of the heavy elements (for instance of oxygen as mentioned in Sect. 3.2). The second is the time delay distribution of SNIa and its overall normalization relative to the core collapse rate, which dictates when iron will be released into the ISM and therefore can be incorporated into newly formed stars. All the simulations discussed in this paper were performed with the fiducial setup in Vogelsberger et al. (2013), but in principle it is possible to act on both factors to reconcile the simulation results with the observational constraints. Also, the efficiency with which metals are transported into the CGM by galactic winds (which in

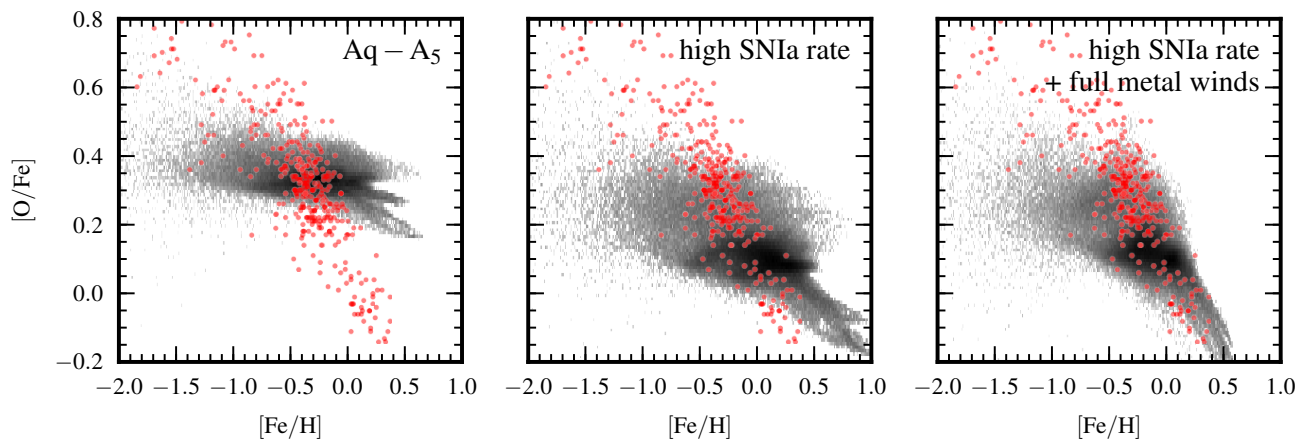


Figure 10. The same as Fig. 8 but showing the $[O/Fe] - [Fe/H]$ plane for the Aq-A-5 halo with three different parametrization of type Ia SNe and wind metal loading: our fiducial set-up (left panel), a simulation with an increased normalization (~ 4 times) in the time delay distribution of SNIa (middle panel) and a model that adds to the higher SNIa normalization fully metal-loaded winds. The increased SNIa rate in the middle and right panels results in a greater iron production that lowers the $[O/Fe]$ values with respect to the fiducial case. Also, the anti-correlation between oxygen and iron content in the stellar component starts to emerge more clearly at high metallicities. In particular, the model that allows for fully metal-loaded outflows is now able to match the trend observed in the Milky Way.

our model is regulated by their metal loading) can play a significant role.

We explore these issues in Fig. 10, where we present again the $[O/Fe]-[Fe/H]$ relation for the Aq-A-5 halo for three different models: our fiducial set-up (left panel), a simulation which uses a higher (~ 4 times) normalization of SNIa rate (middle panel) and a model that in addition to the higher SNIa rate allows for fully metal-loaded winds (right panel), that is winds loaded with all the metal mass of their parent gas cell⁴. The suggested increase in the normalization of the SNIa rate contains two factors, one is from changing the fiducial value of the model parameter from 1.3×10^{-3} (Maoz et al. 2012) to $2.5 \times 10^{-3} [\text{SN } M_{\odot}^{-1}]$, and another factor of about 2 arises from re-defining the SNIa rate parameter as the total number of SNIa per solar mass that explode in the stellar population over a Hubble time ($\simeq 13.56$ Gyr for this simulation set). In Vogelsberger et al. (2013), instead, the upper limit of the normalization integral for the SNIa delay time distribution was taken as infinite. Due to the shallowness of the adopted power law for the SNIa time delay distribution (the power law index is $s = -1.12$), there is then approximately a factor of 2 between these normalization conventions.

From Fig. 10 it can be seen that the increased number of SNIa events in the last two models leads to a higher iron production and therefore to smaller values of the $[O/Fe]$ abundance. More interestingly, a clear anti-correlation between the iron and oxygen content starts to appear at the high-metallicity end. In particular, the model that allows

for fully metal-loaded winds provides an impressively good match of the data for the Milky Way. We explicitly checked that the models with increased SNIa rates yield consistent results for what concerns the galaxy properties examined in MPS14. We found no significant systematic differences except a somewhat higher SFR at late times (an expected trend due to the enhanced cooling of the gas caused by the slightly higher metal production of these simulations) that makes the galaxies appear slightly bluer than in our default run.

The other important mismatch between our simulations and the observations is the presence of only a shallow radial metallicity gradient in the stellar component. A possible explanation for this result is that our discs may suffer from an excessive radial migration of stellar orbits that can considerably reduce any pre-existing radial metallicity gradient, an issue that we will fully explore in future work (Yurin et al., in prep.). An alternative explanation to be considered is that the material from which stars are born is too metal-rich, as a consequence of the strong stellar feedback included in our calculations. It is fairly well established by chemical evolution models of our Galaxy (e.g., Chiappini et al. 2001) that accretion of low-metallicity gas is needed to sustain its current SFR and to match its chemical signatures. In our simulations discs form in an inside-out fashion with gas accretion occurring preferentially at disc edges (see Figs. 9 and 10 in MPS14). In such a scenario, the accretion of relatively metal-poor material would naturally lead to a gradient in the star metallicities if radial migration of stars is not particularly strong. However, as we have discussed above, the material outside the disc has roughly solar metallicity and this similarity in chemical composition with the stellar component might cause a considerable flattening of the expected metallicity gradient. This explanation about the flatness of the stellar metallicity gradient is in line with what is discussed by Gibson et al. (2013) in cosmological simulations of galaxy formation of Milky Way-type objects.

⁴ Note that also in the case of full metal loading the ISM of the galaxy will contain metals, since the generation of wind particles in our model is done on a cell-by-cell basis (for details see Vogelsberger et al. 2013). The fact that the ISM retains metals is also apparent from the right panel of Fig. 10, which shows that the galactic stellar component has stars with solar or slightly super-solar iron content.

In their sample of simulated galaxies these authors find that strong stellar feedback models lead to flat metallicity gradients, an effect that they ascribe to the effectiveness of strong feedback in enriching the CGM and in redistributing this metal-enriched material – that fuels late-time star formation – on large scales.

5 SUMMARY AND CONCLUSIONS

In this paper, we have investigated the properties of the CGM and the metal content of the stars comprising the central galaxy in eight cosmological ‘zoom-in’ simulations of Milky Way-sized haloes taken from the ‘Aquarius’ initial condition set. The simulations were performed with the moving-mesh code AREPO combined with a comprehensive model for galaxy formation physics, which includes, in addition to galactic winds, metal cooling, a self-consistent treatment of the stellar evolution and the associated mass and metal return to the gaseous phase, as well as AGN feedback. The simulations lead to the formation of realistic disc-dominated galaxies whose properties agree quite well with the scaling relations and the observed features of late-type systems. The main findings of our analysis can be summarized as follows:

(i) galactic winds are the main channel for metal enrichment of the CGM as can be inferred from the bipolar morphology (induced by our wind model) of the distribution of the heavy elements in the halo;

(ii) the circum-galactic regions of all the simulated galaxies are substantially metal enriched by the winds that in some cases can transport up to 40% of the total metals beyond the virial radius of the enclosing halo;

(iii) the average mass-weighted metallicity of the CGM is $\sim Z_{\odot}$ and shows a slowly declining trend with radius;

(iv) the density profile and the total mass of the diffuse circum-galactic gas are in agreement with Galactic and L_* galaxies observational constraints and the mass contained in this gas reservoir is a significant fraction of the baryon budget of the halo, although it is in general not sufficient to make the halo baryonically closed;

(v) winds also alter the thermal state of the CGM and supply an energy input capable of sustaining its radiative losses;

(vi) disc and bulge stars show a rather different metallicity distribution with disc stars more metal rich and more narrowly distributed around their metallicity peak (at about Z_{\odot}) than bulge stars;

(vii) stars in the central galaxy exhibit a declining metallicity profile as a function of galactocentric radius, however this gradient is too weak when compared to Galactic observations;

(viii) the relation between oxygen over iron abundance and metallicity in the stellar component shows a trend which is too shallow with respect to Galactic observations; the oxygen vs iron abundance can be reconciled with observations by slightly changing the parameters describing the time delay distribution of SNIa events and the efficiency with which winds transport metals from the central galaxy to the CGM.

It is worth pointing out that the free parameters of our galaxy formation physics model, which are primarily those

determining the strength of the galactic winds, were set to match the final stellar mass of the galaxy and not the properties of the diffuse circum-galactic gas and its metal enrichment properties or those of stars comprising the central galaxy. Therefore, the results listed above are genuine predictions of our galaxy formation model for these properties in late-type galaxies, which can thus be used to check the consistency of the model with constraints that are independent from those considered to set the parameters. The outcome of the analysis carried out in this work suggests that our model can satisfactorily predict the general properties of the circum-galactic medium associated with late-type systems and the metal content of stars contained within the central galaxy. However, at a more detailed level of comparison with the observations discrepancies with the data start to emerge. These discrepancies are signaling deficiencies in our parameterization of the supernova type Ia rate, and possibly also in our phenomenological galactic wind implementation. Resolving these tensions in refined theoretical simulation models will be very helpful in further clarifying the connection between galaxies and their circum-galactic environment as well as for understanding the implications of this connection for galactic evolution.

ACKNOWLEDGEMENTS

We thank an anonymous referee for her/his thoughtful comments and suggestions. We also thank Andrea Gatto for making his routines to generate coronal profiles available to us and Lars Hernquist, Mark Vogelsberger and Till Sawala for useful discussions. FM and VS acknowledge support by the DFG Research Centre SFB-881 ‘The Milky Way System’ through project A1. This work has also been supported by the European Research Council under ERC-StG grant EXAGAL-308037 and by the Klaus Tschira Foundation. Part of the simulations of this paper used the superMUC system at the Leibniz Computing Centre, Garching, under the project PR85JE of the Gauss Centre for Supercomputing, Germany.

REFERENCES

- Abadi M. G., Navarro J. F., Steinmetz M., Eke V. R., 2003, *ApJ*, 591, 499
- Agertz O., Teyssier R., Moore B., 2011, *MNRAS*, 410, 1391
- Anderson M. E., Bregman J. N., 2010, *ApJ*, 714, 320
- Anderson M. E., Bregman J. N., Dai X., 2013, *ApJ*, 762, 106
- Asplund M., Grevesse N., Sauval A. J., Scott P., 2009, *ARA&A*, 47, 481
- Aumer M., White S. D. M., Naab T., Scannapieco C., 2013, *MNRAS*, 434, 3142
- Balogh M. L., Pearce F. R., Bower R. G., Kay S. T., 2001, *MNRAS*, 326, 1228
- Barker M. K., Sarajedini A., Geisler D., Harding P., Schommer R., 2007, *AJ*, 133, 1138
- Battaglia G., Helmi A., Morrison H., Harding P., Olszewski E. W., Mateo M., Freeman K. C., Norris J., Shtetman S. A., 2005, *MNRAS*, 364, 433

- Bensby T., Feltzing S., Lundström I., Ilyin I., 2005, *A&A*, 433, 185
- Boylan-Kolchin M., Bullock J. S., Sohn S. T., Besla G., van der Marel R. P., 2013, *ApJ*, 768, 140
- Boylan-Kolchin M., Springel V., White S. D. M., Jenkins A., 2010, *MNRAS*, 406, 896
- Boylan-Kolchin M., Springel V., White S. D. M., Jenkins A., Lemson G., 2009, *MNRAS*, 398, 1150
- Brooks A. M., Solomon A. R., Governato F., McCleary J., MacArthur L. A., Brook C. B. A., Jonsson P., Quinn T. R., Wadsley J., 2011, *ApJ*, 728, 51
- Chabrier G., 2003, *ApJ*, 586, L133
- Chiappini C., Matteucci F., Romano D., 2001, *ApJ*, 554, 1044
- Coşkunoglu B., Ak S., Bilir S., Karaali S., Önal Ö., Yaz E., Gilmore G., Seabroke G. M., 2012, *MNRAS*, 419, 2844
- Dehnen W., McLaughlin D. E., Sachania J., 2006, *MNRAS*, 369, 1688
- Faucher-Giguère C.-A., Lidz A., Zaldarriaga M., Hernquist L., 2009, *ApJ*, 703, 1416
- Gatto A., Fraternali F., Read J. I., Marinacci F., Lux H., Walch S., 2013, *MNRAS*, 433, 2749
- Genel S., Vogelsberger M., Nelson D., Sijacki D., Springel V., Hernquist L., 2013, *MNRAS*, 435, 1426
- Gibson B. K., Pilkington K., Brook C. B., Stinson G. S., Bailin J., 2013, *A&A*, 554, A47
- Gratton R. G., Carretta E., Claudi R., Lucatello S., Barbieri M., 2003, *A&A*, 404, 187
- Guedes J., Callegari S., Madau P., Mayer L., 2011, *ApJ*, 742, 76
- Hodges-Kluck E. J., Bregman J. N., 2013, *ApJ*, 762, 12
- Hopkins P. F., Keres D., Onorbe J., Faucher-Giguère C.-A., Quataert E., Murray N., Bullock J. S., 2013, *ArXiv e-prints*, 1311.2073
- Hopkins P. F., Quataert E., Murray N., 2011, *MNRAS*, 417, 950
- Lehner N., Howk J. C., Thom C., Fox A. J., Tumlinson J., Tripp T. M., Meiring J. D., 2012, *MNRAS*, 424, 2896
- Li Y.-S., White S. D. M., 2008, *MNRAS*, 384, 1459
- Macciò A. V., Dutton A. A., van den Bosch F. C., 2008, *MNRAS*, 391, 1940
- Magrini L., Stanghellini L., Villaver E., 2009, *ApJ*, 696, 729
- Maoz D., Mannucci F., Brandt T. D., 2012, *MNRAS*, 426, 3282
- Marinacci F., Binney J., Fraternali F., Nipoti C., Ciotti L., Londrillo P., 2010, *MNRAS*, 404, 1464
- Marinacci F., Fraternali F., Nipoti C., Binney J., Ciotti L., Londrillo P., 2011, *MNRAS*, 415, 1534
- Marinacci F., Pakmor R., Springel V., 2014, *MNRAS*, 437, 1750 (MPS14)
- Martin C. L., Kobulnicky H. A., Heckman T. M., 2002, *ApJ*, 574, 663
- Miller M. J., Bregman J. N., 2013, *ApJ*, 770, 118
- Pakmor R., Marinacci F., Springel V., 2014, *ApJ*, 783, L20
- Pakmor R., Springel V., 2013, *MNRAS*, 432, 176
- Peeples M. S., Werk J. K., Tumlinson J., Oppenheimer B. D., Prochaska J. X., Katz N., Weinberg D. H., 2014, *ApJ*, 786, 54
- Pettini M., Steidel C. C., Adelberger K. L., Dickinson M., Gialalisco M., 2000, *ApJ*, 528, 96
- Planck Collaboration: Ade P. A. R., Aghanim N., Armitage-Caplan C., Arnaud M., Ashdown M., Atrio-
- Barandela F., Aumont J., Baccigalupi C., Banday A. J., et al. 2013, *ArXiv e-prints*, 1303.5076
- Prochaska J. X., Weiner B., Chen H.-W., Cooksey K. L., Mulchaey J. S., 2011, *ApJS*, 193, 28
- Puchwein E., Springel V., 2013, *MNRAS*, 428, 2966
- Rahmati A., Pawlik A. H., Raičević M., Schaye J., 2013, *MNRAS*, 430, 2427
- Ramya P., Reddy B. E., Lambert D. L., 2012, *MNRAS*, 425, 3188
- Reddy B. E., Tomkin J., Lambert D. L., Allende Prieto C., 2003, *MNRAS*, 340, 304
- Renaud F., Bournaud F., Emsellem E., Elmegreen B., Teyssier R., Alves J., Chapon D., Combes F., Dekel A., Gabor J., Hennebelle P., Kraljic K., 2013, *MNRAS*, 436, 1836
- Rudolph A. L., Fich M., Bell G. R., Norsen T., Simpson J. P., Haas M. R., Erickson E. F., 2006, *ApJS*, 162, 346
- Sakamoto T., Chiba M., Beers T. C., 2003, *A&A*, 397, 899
- Sales L. V., Marinacci F., Springel V., Petkova M., 2014, *MNRAS*, 439, 2990
- Sanders N., Caldwell N., McDowell J., 2010, in *American Astronomical Society Meeting Abstracts #215 Vol. 36 of Bulletin of the American Astronomical Society, The Abundance Distribution In M31 From Optical Spectroscopy Of HII Regions And Planetary Nebulae*. p. 415.33
- Savage B. D., Sembach K. R., Wakker B. P., Richter P., Meade M., Jenkins E. B., Shull J. M., Moos H. W., Sonneborn G., 2003, *ApJS*, 146, 125
- Scannapieco C., Tissera P. B., White S. D. M., Springel V., 2008, *MNRAS*, 389, 1137
- Scannapieco C., Wadepuhl M., Parry O. H., Navarro J. F., Jenkins A., Springel V., Teyssier R., et al. 2012, *MNRAS*, 423, 1726
- Scannapieco C., White S. D. M., Springel V., Tissera P. B., 2009, *MNRAS*, 396, 696
- Sembach K. R., Wakker B. P., Savage B. D., Richter P., Meade M., Shull J. M., Jenkins E. B., Sonneborn G., Moos H. W., 2003, *ApJS*, 146, 165
- Sijacki D., Vogelsberger M., Kereš D., Springel V., Hernquist L., 2012, *MNRAS*, 424, 2999
- Simpson C. M., Bryan G. L., Johnston K. V., Smith B. D., Mac Low M.-M., Sharma S., Tumlinson J., 2013, *MNRAS*, 432, 1989
- Soto K. T., Martin C. L., Prescott M. K. M., Armus L., 2012, *ApJ*, 757, 86
- Springel V., 2005, *MNRAS*, 364, 1105
- Springel V., 2010, *MNRAS*, 401, 791
- Springel V., Di Matteo T., Hernquist L., 2005, *MNRAS*, 361, 776
- Springel V., Hernquist L., 2003, *MNRAS*, 339, 289
- Springel V., Wang J., Vogelsberger M., Ludlow A., Jenkins A., Helmi A., Navarro J. F., Frenk C. S., White S. D. M., 2008, *MNRAS*, 391, 1685
- Springel V., White S. D. M., Jenkins A., Frenk C. S., Yoshida N., Gao L., Navarro J., Thacker R., Croton D., Helly J., Peacock J. A., Cole S., Thomas P., Couchman H., Evrard A., Colberg J., Pearce F., 2005, *Nature*, 435, 629
- Stinson G. S., Bailin J., Couchman H., Wadsley J., Shen S., Nickerson S., Brook C., Quinn T., 2010, *MNRAS*, 408, 812

- Stinson G. S., Brook C., Macciò A. V., Wadsley J., Quinn T. R., Couchman H. M. P., 2013, *MNRAS*, 428, 129
- Stinson G. S., Brook C., Prochaska J. X., Hennawi J., Shen S., Wadsley J., Pontzen A., Couchman H. M. P., Quinn T., Macciò A. V., Gibson B. K., 2012, *MNRAS*, 425, 1270
- Strickland D. K., Heckman T. M., Colbert E. J. M., Hoopes C. G., Weaver K. A., 2004, *ApJ*, 606, 829
- Strickland D. K., Stevens I. R., 2000, *MNRAS*, 314, 511
- Toro E. F., 1999, *Riemann Solvers and Numerical Methods for Fluid Dynamics: A Practical Introduction*. Springer-Verlag
- Torrey P., Vogelsberger M., Genel S., Sijacki D., Springel V., Hernquist L., 2014, *MNRAS*, 438, 1985
- Vogelsberger M., Genel S., Sijacki D., Torrey P., Springel V., Hernquist L., 2013, *MNRAS*, 436, 3031
- Vogelsberger M., Genel S., Springel V., Torrey P., Sijacki D., Xu D., Snyder G., Bird S., Nelson D., Hernquist L., 2014, *Nature*, 509, 177
- Vogelsberger M., Sijacki D., Kereš D., Springel V., Hernquist L., 2012, *MNRAS*, 425, 3024
- Werk J. K., Prochaska J. X., Tumlinson J., Peeples M. S., Tripp T. M., Fox A. J., Lehner N., Thom C., O’Meara J. M., Ford A. B., Bordoloi R., Katz N., Tejos N., Oppenheimer B. D., Davé R., Weinberg D. H., 2014, *ArXiv e-prints*, 1403.0947
- Xue X. X., Rix H. W., Zhao G., Re Fiorentin P., Naab T., Steinmetz M., van den Bosch F. C., Beers T. C., Lee Y. S., Bell E. F., Rockosi C., Yanny B., Newberg H., Wilhelm R., Kang X., Smith M. C., Schneider D. P., 2008, *ApJ*, 684, 1143